Materials Today Physics 22 (2022) 100571

Contents lists available at ScienceDirect

Materials Today Physics

journal homepage: https://www.journals.elsevier.com/materials-today-physics

Achieving synergistic performance through highly compacted microcrystalline rods induced in Mo doped GeTe based compounds

Safdar Imam [a, b], Khasim Saheb Bayikadi [b], Mohammad Ubaid [c], V.K. Ranganayakulu [b], Sumangala Devi [b], Bhalchandra S. Pujari [d], Yang-Yuan Chen [b], Li-Chyong Chen [e], Kuei-Hsien Chen [f], Feng-Li Lin [a, **], Raman Sankar [b, *]

[a] Department of Physics, National Taiwan Normal University, Taipei 11677, Taiwan
[b] Institute of Physics, Academia Sinica, Taipei 11529, Taiwan
[c] Department of Physics, Jamia Millia Islamia, New Delhi, 110025, India
[d] Department of Scientific Computing, Modeling & Simulation, Savitribai Phule Pune University, Pune, India
[e] Center for Condensed Matter Sciences, National Taiwan University, Taipei, Taiwan
[f] Institute of Atomic and Molecular Sciences, Academia Sinica, Taipei 10617, Taiwan

ARTICLE INFO

Article history:
Received 22 September 2021
Received in revised form
1 November 2021
Accepted 10 November 2021
Available online 17 November 2021

Keywords:
GeTe
Microcrystalline rods
Carrier concentration optimization
Thermal conductivity
Figure of merit

ABSTRACT

Among the lead-free thermoelectric material, germanium telluride (GeTe) has been extensively investigated due to its high thermoelectric performance (ZT) in mid-temperature; however, high p-type carrier density (~10^{21} cm^{-3}) hinder its suitability for higher ZT. To enhance the thermoelectric performance of the environmentally favorable GeTe, we explored the Mo doping significantly optimizes the carrier concentration along with uniquely unveiled microcrystalline rods accompanying compact grain boundaries, high-density planar defects, and point defects effectuating all-frequency phonon scattering yields to lower down the thermal conductivity. Furthermore, Sb/Bi co-doping with Mo at the Ge sites predominantly reduces the carrier concentration and thermal conductivity to attain a higher ZT. The co-doping of Bi manifested a more prominent role in achieving the highest ZT of ~2.3 at 673 K for the sample composition with $Ge_{0.89}Mo_{0.01}Bi_{0.1}Te$. This study demonstrates an exciting hidden aspect of microstructural modification by forming highly dense microcrystalline rods through Mo doping to achieve high performance in the GeTe system.

1. Introduction

In the 21st-century, energy sustainability is an essential technological difficulty. Increasing cognizance and distressing attention to nature and energy crises have driven us to further improve materials engineering for energy harvesting. Thermoelectricity is a popularly acknowledged subject due to its electrical power generation with green technology strategies. Thermoelectric (TE) materials can transform temperature gradient into electrical energy based on the Seebeck effect. Its low energy transformation efficiency limits the extended utilization of TE technology; however, they have a potential role in current and future energy management due to the advancement in the research [1–8]. The dimensionless figure-of-merit can estimate the performance of TE materials, $ZT = \sigma S^2 T/\kappa$, where σ, S, κ, and T are the electrical conductivity, Seebeck coefficient, total thermal conductivity, and absolute temperature, respectively. Where σS^2 is known as the power factor (PF), κ is constituted of the electronic κ_{ele} and lattice κ_{lat} parts of thermal conductivity. However, improving a material's ZT is a vast hurdle for the TE materials as it greatly depends on three interdependent parameters, i.e., S, σ and κ. The notable efforts to improve the TE power factor (σS^2) and suppress the κ have been made, necessitating criteria to achieve high ZT [9–11]. Enhancement of PF is significantly improved via modulated doping [12–14], band engineering [15–18], magnetic enhancement [19,20], quantum confinement [21], and phase transition [22,23], etc. Additionally, the thermal conductivity of the TE materials can be efficiently reduced through various approaches, i.e., phonon scattering [24–26], defect engineering [27,28], intrinsic bond anharmonicity

* Corresponding author.
** Corresponding author.
E-mail addresses: fengli.lin@gmail.com (F.-L. Lin), sankarraman@gate.sinica.edu.tw (R. Sankar).

https://doi.org/10.1016/j.mtphys.2021.100571
2542-5293/

[29–32],and secondary phases [33–35] etc. An ideal TE material must uncover an equilibrium between the conflicting requirements of ZT parameters.

In recent years, germanium telluride (GeTe) based TE materials underwent accelerated research attention for mid-temperature TE utilization and are suitable for replacing conventional high-performance PbTe due to toxicity concerns [17,36,37]. The pristine GeTe exists in the rhombohedral phase at room temperature (RT) (space group R3m) and converts into the cubic phase at the high temperature (space group Fm $\bar{3}$ m). The r-GeTe structure is a slightly distorted rock-salt system along its [111] direction, and this symmetry breaking leads to the change in c-GeTe and r-GeTe's band structures [38–40]. Nevertheless, a very high p-type carrier density (~10^{21} cm^{-3}) due to the small formation energy of Ge vacancies restricts the Seebeck coefficient to a low value, which is an unfavorable condition for achieving a high ZT. Hence, several earlier investigations for enhancing the TE performance of GeTe focuses on optimizing the carrier concentration [38,39,41]. Near room and mid-temperature TE applications, GeTe based materials are encouraging competitors with reasonable further progressions, and our analysis will provide a step towards that progress.

Chemical doping is one of the primary methods to improve electric transport properties and reduce thermal conductivity in the GeTe system. In the concern above, doping/substitution/alloying of aliovalent or electron donor elements compositions have been reported to optimize numerous factors influential for the enhanced TE performance. The Ge site was replaced by various dopants inside the GeTe system, such as Bi [42], Sb [43,44], Pb [45], In [41,46], Al [47], Cr [48], Ag [49], Mn [50], etc., and an enhancement in ZT was achieved for these singly doped GeTe. Furthermore, co-doped compositions with Sb/Bi into the Ge side have been demonstrated to reduce the hole carrier concentration and enhance the ZT compared to the other single doped GeTe systems, such as Sb and Se [51], Bi and Ti [52], Bi and In [53], Bi/Sb and Cr [48], Sb and P [35], Sb and Bi [54], Bi and Cd [55], Bi and Pb [38], Sb and Ga [56], Sb and Pb [57], Sb and Mn [22,50], Bi and Mn [22], Sb and Zn [58], etc. The transition elements (Y, Zr, Hf, V, Nb, Mo, and Ru) and rare-earth (La and Pr) elements were explored as an efficient dopant in the GeTe system to optimize and enhance the ZT by *B. Srinivasan* et al. [59] Furthermore, *W. Gao* et al. [60], showed a decrease in carrier concentration and induced band convergence to achieve a high power factor by Yttrium (Y) doping, leading to an enhanced ZT. Recently; the versatile role of Vanadium (V) was explored by the solute drag effect, stacking faults, and Ge nano precipitates caused by planar defects along with optimized carrier concentration, which enables the low thermal conductivity and a peak ZT value of >2.1 at 773 K by *Q. Sun* et al. [61] The search of Pb-free doping and intriguing TE outcomes of the GeTe systems mentioned earlier motivated us to further study these element's hidden potentials for exciting aspects of TE properties.

In this study, we chose Molybdenum (Mo), a widely used transition element, for further investigations and demonstrated Mo's role in strengthening the TE properties of GeTe. The density functional theory (DFT) calculations and TE transport properties experiments were performed to study the influence of Mo doping on the Ge site of the GeTe system. DFT computations predict the additional dopant/impurity states induced by Mo-doping. Mo doping sharply decreased the carrier concentration, e.g., from 8.28 × 10^{20} cm^{-3} (pristine GeTe) to 5.24 × 10^{20} cm^{-3} for $Ge_{0.97}Mo_{0.03}Te$ with a slight increase in the Seebeck at room temperature. The simultaneous reduction in κ is correlated with optimized carrier concentration, multi-scale lattice deformation, verified by extensive microstructural studies, emphasized by microcrystalline rods (MCRs), high-density planar defects, nano strained domains, strained stacking faults, point defects, herringbone, strengthening all-frequency phonon scattering. Moreover,

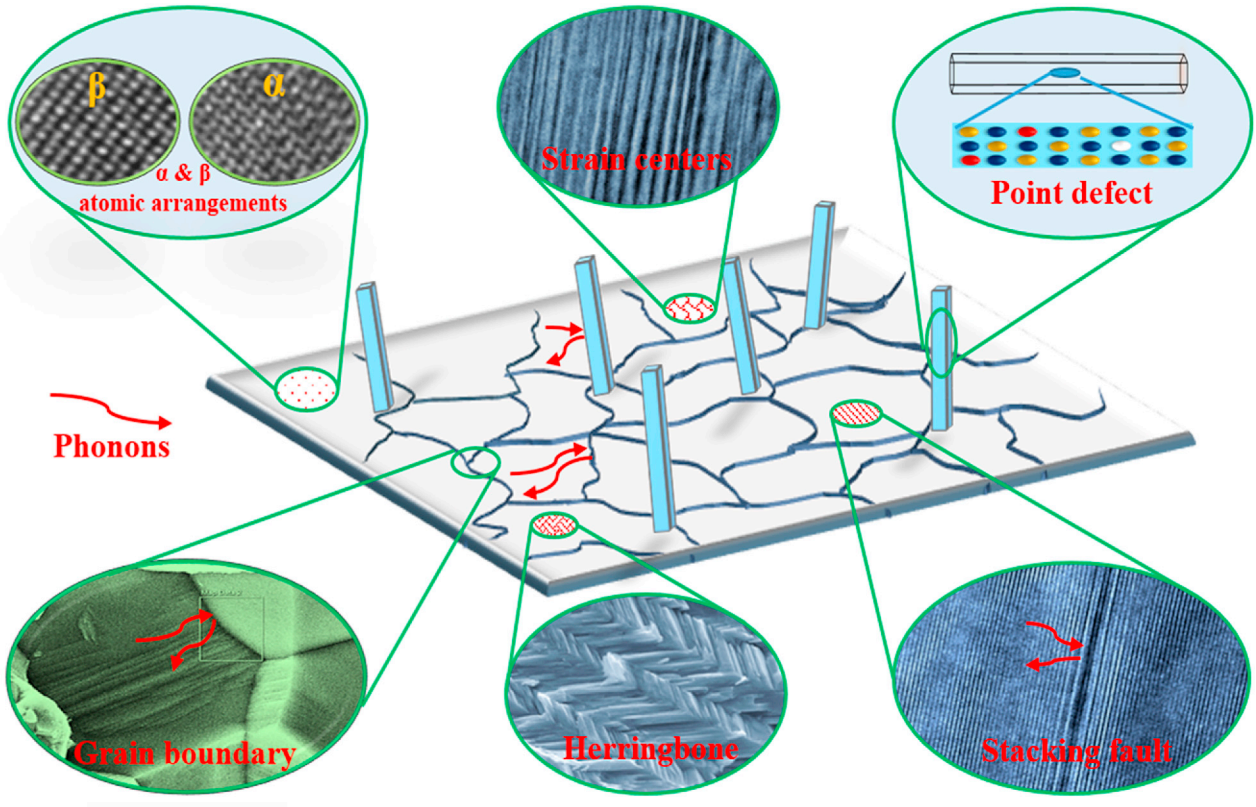

Fig. 1. Schematic diagram of different phonon scattering centers observed in Mo doped GeTe thermoelectric systems.

co-doping of Sb/Bi with Mo at the Ge sites primarily decreases the carrier concentration (n) and thermal conductivity (κ) to achieve a higher ZT. The co-doping of Sb/Bi demonstrated a prominent role with a maximum ZT of ~2.14 and ~2.3 at 673 K for the samples of $Ge_{0.89}Mo_{0.01}Sb_{0.1}$Teand $Ge_{0.89}Mo_{0.01}Bi_{0.1}Te$, respectively. This work reports one of the highest TE performances among the transition metal co-doping in the mid-temperature range. The synergistic performance with an ultralow thermal conductivity has been achieved primarily due to microcrystalline-assisted grain boundary formations, a possible pathway for reducing the thermal conductivity. Fig. 1 shows the schematic diagram of different scattering centers in Mo doped GeTe systems, which helps the reduction in κ_{lat}, and overall thermal conductivity reached to an ultralow, owing to a highly disordered network formation to hinder the phonon transport.

2. Result and discussion

2.1. Crystal symmetry and microstructure analysis

GeTe has been explored as a promising TE material in the mid-temperature range. The pristine GeTe transforms from rhombohedral phase near RT to cubic phase at the higher temperature, a reversible transformation, as shown in Fig. 2 (a). To investigate the structural phases of the Mo doped GeTe samples, we performed powder X-ray diffraction (XRD) analysis at RT, and the outcomes are presented in Fig. 2 (b). The XRD diffraction patterns for Mo doped GeTe are well-matched with the r-GeTe (ICSD-98-005-6038), implying that Mo doping does not significantly alter the RT crystal structure for the pristine GeTe. A gradual merging of two peaks in the 2θ range ~ 41–45° indicates the crystal structure of $Ge_{0.89}Mo_{0.01}(Sb/Bi)_{0.1}Te$ transforms from the rhombohedral to a pseudo-cubic structure at RT. A single peak around 2θ: ~ 41–45° shows a cubic structure, which significantly influences the Seebeck coefficient [43], which is also reflected in the TE performances of the Sb/Bi co-doped samples. In extension, an inadequate amount of impurity phase of $MoTe_2$ (ICSD-73-1650) is observed in $Ge_{1-x}Mo_xTe$ for x = 0.03, & 0.04 samples, showing that the Mo solubility in the GeTe system is ~2%, which is further confirmed with the SEM-EDS analysis. To further explore the influence of Mo doping on the structures of GeTe, we performed differential scanning calorimetry (DSC) studies, as shown in Fig. 2 (c). Rhombohedral (R3m) to cubic symmetry (Fm $\bar{3}$ m) structural phase transition for $Ge_{0.99}Mo_{0.01}Te$ observed near ~ 630 K, suppressed compared to the pristine GeTe, which can be seen as an endothermic peak. This endothermic peak was further decreased for $Ge_{0.89}Mo_{0.01}Sb_{0.1}Te$ to ~ 600 and ~ 590 K for $Ge_{0.89}Mo_{0.01}Bi_{0.1}Te$. It is essential to decrease the phase transition temperature for long-term thermal stability and improve TE performance over a wide temperature range [22,23]. Fig. 2 (d) represents the synchrotron X-ray diffraction at different temperatures for the $Ge_{0.89}Mo_{0.01}Bi_{0.1}Te$ sample, showing rhombohedral to simple cubic phase transformation occurs at ~600 K. The insets near 300 and 773 K represent

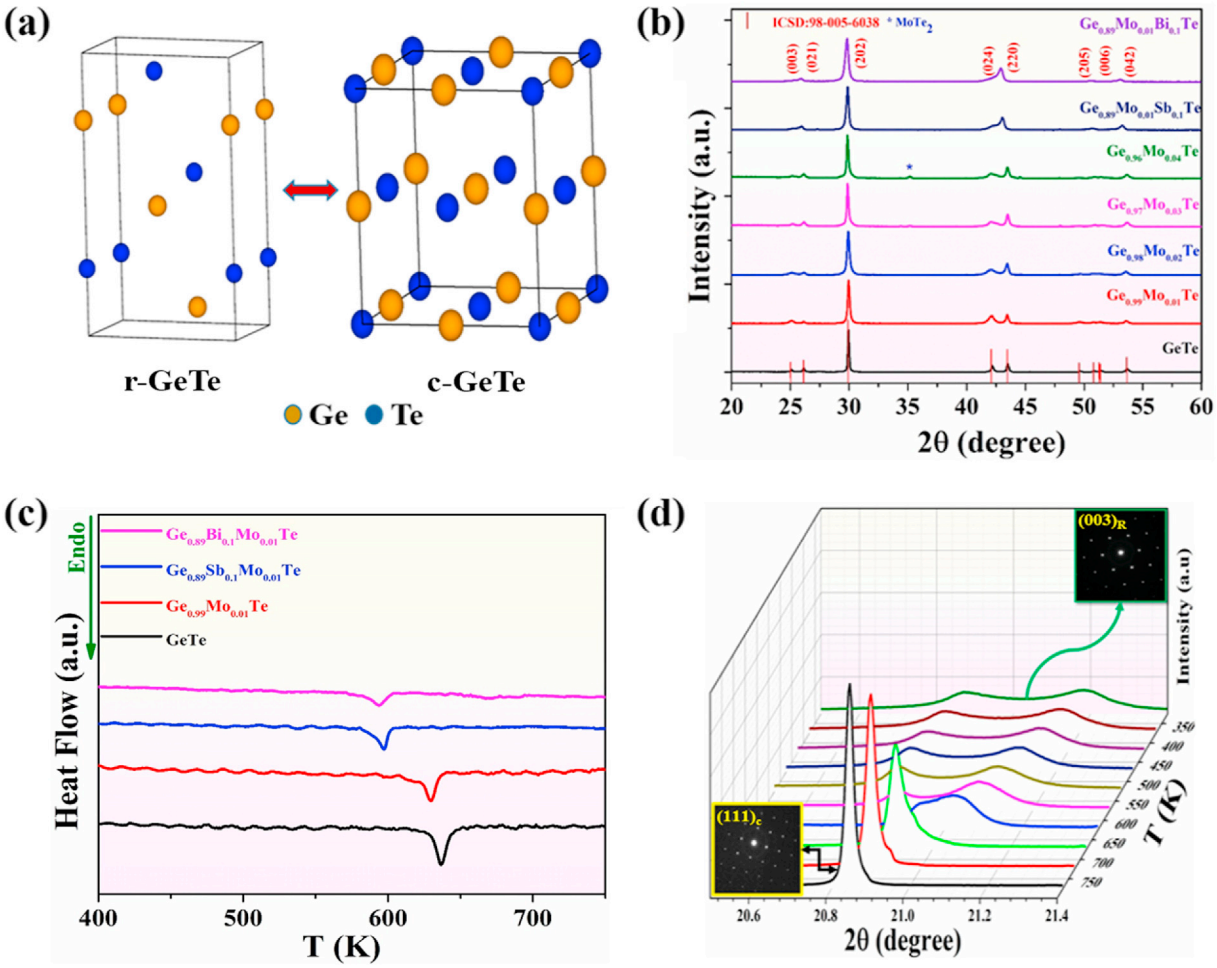

Fig. 2. (a) schematic diagram of r-GeTe and c-GeTe, (b) powder XRD patterns of Mo doped GeTe compounds, (c) differential scanning calorimetry analysis, and (d) temperature-dependent XRD patterns of $Ge_{0.89}Mo_{0.01}Bi_{0.1}Te$ sample: top and bottom insets reveal the SAED patterns of rhombohedral and cubic symmetries, respectively.

the Selective Area Electron Diffraction (SAED) pattern, intimating the rhombohedral $(003)_R$ plane and cubic $(111)_C$ plane nature of the sample, respectively. The phase transition can be seen from 573 to 673 K, and due to the symmetric cubic structure, the compounds are more electrically conductive than the earlier phase, which is also reflected in all thermoelectric transport properties [62].

2.2. Microstructure characterization

Different microstructural imperfections, such as interfaces, point defects, dislocations, herringbone structure, grain boundaries, act as phonon scattering centers to reduce thermal conductivity with a decrease in κ_{lat} and achieve high-performance in TE materials [44,63]. To further understand the phase composition and illustrate the microstructure, Field Emission Scanning Electron Microscope (FESEM) and Energy Dispersion Spectroscopy (EDS) studies were carried out on all samples. Fig. S1 (a & b) represents the cross-sectional SEM image of the fractural $Ge_{0.99}Mo_{0.01}Te$ sample. Fig. S1 (a) shows the high-density close packing nature and herringbone structure observed with strained boundaries separating each domain. Mo-doping in GeTe matrix increases the grain boundaries density as unveiled in Fig. S1 (b), which can scatter the phonons and further enhance the TE properties via decreasing κ_{lat}. Fig. S1 (c & d) represents the EDS images of the $Ge_{0.97}Mo_{0.03}Te$ and $Ge_{0.96}Mo_{0.04}Te$ samples, respectively, which further confirms the existence of secondary $MoTe_2$ phase impurity in the sample above 2% Mo doping. Fig. 3 (a & b) shows the FESEM images of the $Ge_{0.98}Mo_{0.02}Te$ sample, unveiling the unique MCRs in the sample. The EDS analysis presented in Fig. 3 (c) demonstrates that the distribution of elements in MCRs are uniformly distributed. The similar unique microstructures were also unveiled for the (Bi/Sb) Mo doped GeTe systems, as shown in Fig. 3(d–f) for the $Ge_{0.89}Mo_{0.01}Bi_{0.1}Te$ sample and Fig. 3(g–i) for the $Ge_{0.89}Mo_{0.01}Sb_{0.1}Te$ sample. A uniform elemental distributed MCRs induced high compacted Mo doped GeTe compounds that can create an additional strength to the material property [64]. We believe that these

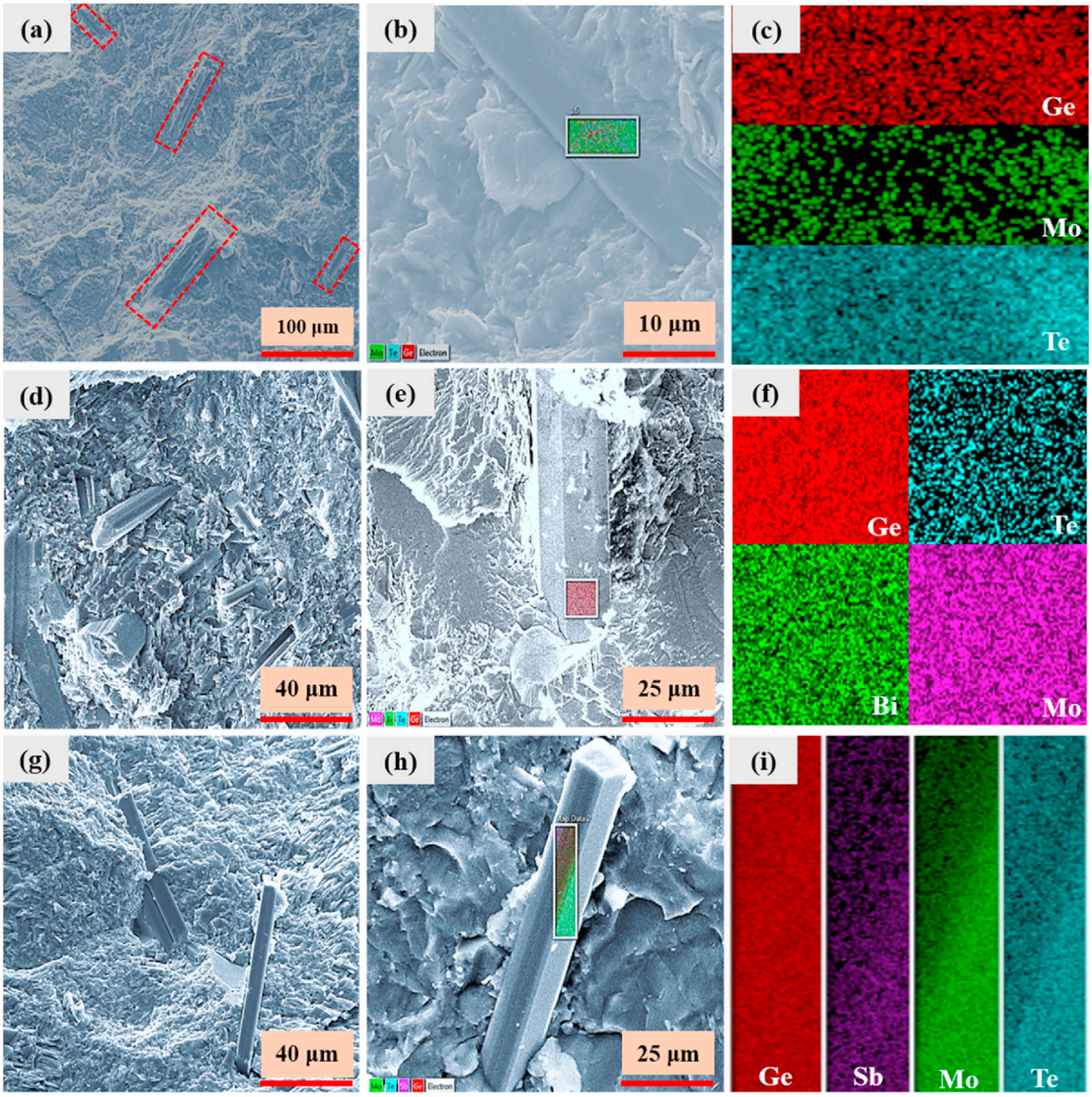

Fig. 3. SEM images of the free fractured surface of the hot-pressed samples: (a & b) $Ge_{0.98}Mo_{0.02}Te$, (d & e) $Ge_{0.89}Mo_{0.01}Bi_{0.1}Te$, (g & h) $Ge_{0.89}Mo_{0.01}Sb_{0.1}Te$ high-density fractural structure along with microcrystalline rods; (c, f & i) elemental mapping of $Ge_{0.98}Mo_{0.02}Te$, $Ge_{0.89}Mo_{0.01}Bi_{0.1}Te$, $Ge_{0.89}Mo_{0.01}Sb_{0.1}Te$ microcrystalline rods, respectively.

MCRs provide the shortest paths for the conduction of charge carriers and create additional grain boundaries along the rods, creating more phonon scattering centers [65]. Fig. S2 (a & b) represent the SEM images of pristine GeTe, and no MCRs were observed. Fig. S2 (c & d), S2 (e & f) and S2 (g & h) represent the cross-sectional SEM images of the fractural $Ge_{0.99}Mo_{0.01}Te$, $Ge_{0.89}Mo_{0.01}Bi_{0.1}Te$ and $Ge_{0.89}Mo_{0.01}Sb_{0.1}Te$, respectively and showing more MCRs compacted dense grain arrangement in an extensive micro areal range. Fig. S2 (h) reveals a highly smooth MCR surface that resembles the rods' highly crystalline and dense quality. Finally, comparative microstructural studies validate the extensive role of Mo doping in GeTe systems for uniquely formed MCRs.

In order to understand the structural and morphological changes, High-Resolution Transition Electron Microscope (HR-TEM) analysis was employed to the hot-pressed samples. Fig. 4 illustrates the detailed TEM analysis of the $Ge_{0.89}Mo_{0.01}Bi_{0.1}Te$ sample, and HR-TEM images were taken on a hot-pressed pellet with sample preparation by Focus Ion Beam cutting (FIB). Fig. 4 (a) represents the strained domains and boundary (yellow box) of the $Ge_{0.89}Mo_{0.01}Bi_{0.1}Te$ sample; inset represents the Fast Fourier Transformation (FFT) of the high-resolution lattice showing (003) plane of the GeTe system. Fig. 4 (b) reveals the stacking fault originating from the highly strained lattice of the Bi/Mo substitute GeTe, and the inset exhibits the lattice disorder (unusual lattice d-spacing) presence in the stacking fault. Fig. 4 (c) shows the herringbone domain structure of the $Ge_{0.89}Mo_{0.01}Bi_{0.1}Te$ sample within the nanoscale range. Fig. 4 (d) explores the HR-TEM image of the highly strained herringbone domains, and the inset represents the magnified view of the $Ge_{0.89}Mo_{0.01}Bi_{0.1}Te$ sample. High crystalline nature represents the hexagonal lattice arrangement of the GeTe system. Atomic substitution disorder (Ge/Mo/Bi) presence in the atomic scale range, a manifestation of the nano strained domains, strained stacking faults in the nanoscale range, and microscale domain boundaries, grain boundaries, and MCRs in the mesoscale range will work as a scattering network for the phonon spectrum [63]. Fig. S3 represents the HR-TEM analysis of the

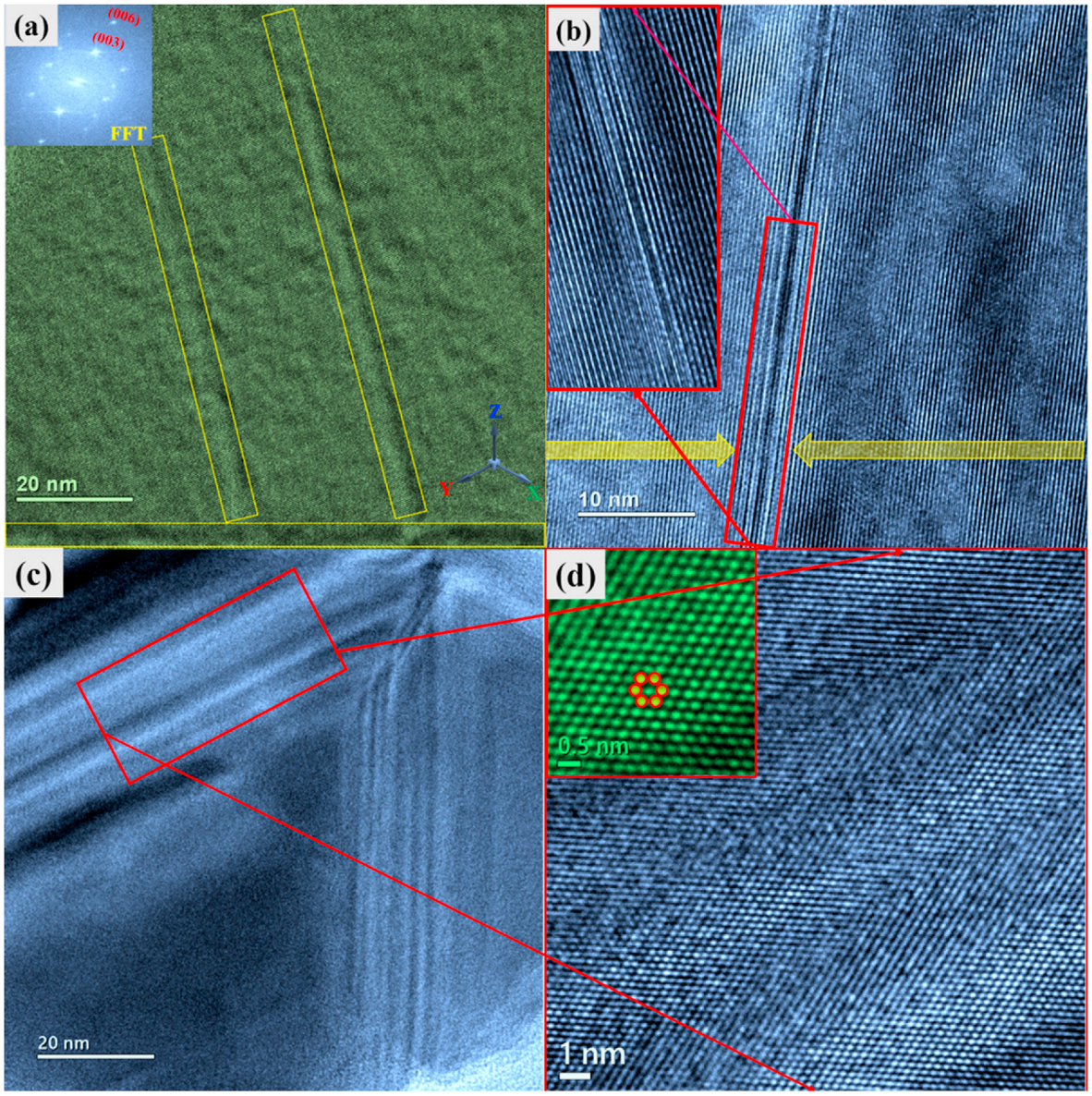

Fig. 4. HR-TEM images of $Ge_{0.89}Mo_{0.01}Bi_{0.1}Te$ sample: (a) strained domains and boundary (yellow box), inset showing FFT of the high-resolution lattice showing (003) plane, (b) highly compressed stacking fault (inset: enlarged view), (c) herringbone domain structure, and (d) highly strained herringbone domains; inset represents the magnified view.

$Ge_{0.89}Mo_{0.01}Sb_{0.1}Te$ sample. Fig. S3 (a) illustrates the strained lattice of the $Ge_{0.89}Mo_{0.01}Sb_{0.1}Te$ sample, and the inset represents the SAED pattern of the pseudo-cubic structure. Fig. S3 (b) reveals the HR-TEM image of the $Ge_{0.89}Mo_{0.01}Sb_{0.1}Te$ sample existed with cubic (green) as well as rhombohedral (red) lattice arrangement highlighted in the rectangular boxes. Fig. S3 (c) shows the highly disordered lattice arrangement of the $Ge_{0.89}Mo_{0.01}Sb_{0.1}Te$ sample along with hexagonal lattice arrangement (rhombohedral lattice). Fig. S3 (d) explores the HR-TEM image of the $Ge_{0.89}Mo_{0.01}Sb_{0.1}Te$ sample with highly crystalline lattice d spacing. The pseudo-cubic nature represents more lattice disorder in the $Ge_{0.89}Mo_{0.01}Sb_{0.1}Te$ sample, which resembles the similar phonon scattering network of the $Ge_{0.89}Mo_{0.01}Bi_{0.1}Te$ sample. Furthermore, all the structural strain analyses from the XRD were calculated and represented in Fig. S4; the peak shift of $(202)_R$ or $(200)_C$ towards the lower angle side represents the Ge vacancy control in GeTe. Phonons with different frequencies can be scattered from scattering centers with different scales. Point defects or different atomic arrangements can scatter the high-frequency phonons, stacking defects, and herringbone can scatter mid-frequency phonons, grain boundaries including the phase boundaries of MCRs can scatter the low-frequency phonons (Fig. 1). All samples create the whole phonon spectrum scattering mechanism from the atomic scale to the mesoscale range, contributing to a low κ_{lat} in the Mo-doped GeTe and Sb/Bi co-doped systems.

2.3. Electronic structure

To investigate the electronic structures of the GeTe system due to Mo doping, DFT calculations were computed and analyzed. Fig. 5 (a & c) shows the electronic band structure (EBS) and density of states (DOS) of the pristine $Ge_{100}Te_{100}$, along Γ-K high symmetry points of the cubic Brillouin zone (BZ). The calculated direct bandgap of c-$Ge_{100}Te_{100}$ is 0.38 eV at L-point and DOS depicted in Fig. 5 (c). Valence and conduction bands near Fermi level (E_F) at E ~ 0 eV predominantly constituted Te $5p^4$ and Ge $4p^2$ orbitals. Furthermore, the calculated EBS and DOS of Mo doped GeTe (c-$Ge_{99}MoTe_{100}$) is shown in Fig. 5 (b) & 5 (d), respectively. Upon Mo doping, the direct bandgap of c-$Ge_{99}MoTe_{100}$ has been increased by 0.08 eV, resulting from the difference between the electronegativity of dopant and Ge/Te atoms. The Mo states are partially occupied and highly localized; hence valence band maximum (VBM) is shown by 0 eV [61]. Upon Mo doping, it can be shown from Fig. 5 (b) that the curvature of the E-K-diagram is decreasing (flatness of bands is increasing), which increases the effective mass and hence the Seebeck coefficient as well. The closely spaced bands and degeneracy in the EBS confine different effective electronic states (impurity states) around the Fermi level (Fig. 5(b)) that is determined by the valance band maximum (VBM) and conduction band minimum (CBM), resulting in enhanced Seebeck coefficient [66–68]. The energy difference between the lowest two CBM of c-

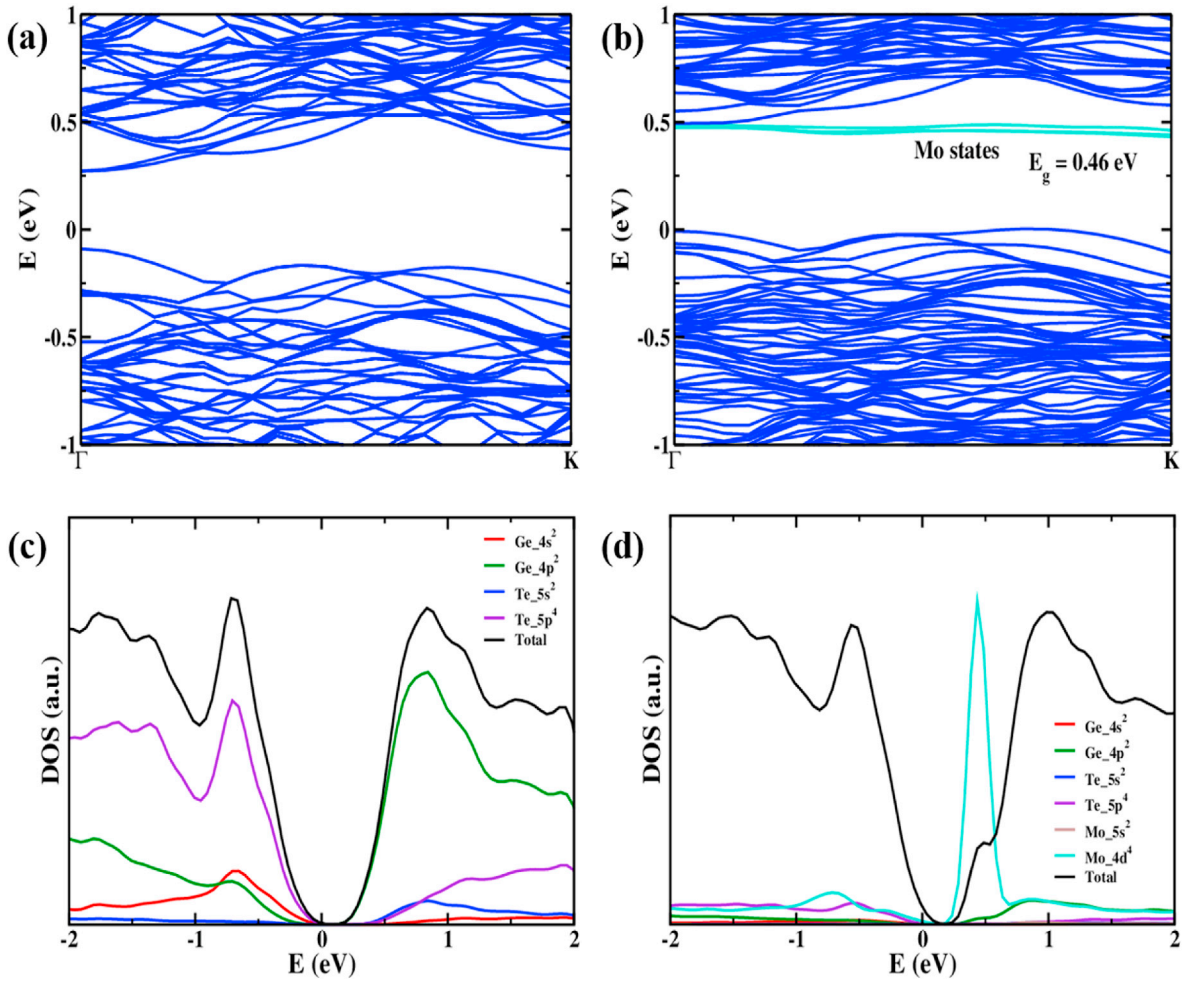

Fig. 5. The calculated band structure for (a) c-$Ge_{100}Te_{100}$ and (b) c-$Ge_{99}MoTe_{100}$; and (c & d) projected DOS for c-$Ge_{100}Te_{100}$ and c-$Ge_{99}MoTe_{100}$. For clear visualization, projected DOS of orbitals are magnified by a factor of 100 and 10 for (c) and (d), respectively. Valence band maximum is pinned at 0 eV.

$Ge_{99}MoTe_{100}$ is 0.008 eV, while the energy difference between the two VBM of c-$Ge_{99}MoTe_{100}$ is 0.01 eV, determining the band degeneracy, as smaller energy difference (less than $K_BT = 0.0259$ eV) between the nearest two bands around the Fermi level results in higher band degeneracy, leading to higher effective DOS [69]. The conduction band is dominated by the combination of Mo-$4d^4$ and Ge-$4p^2$ orbital's, showing strong hybridization between Mo and Ge from 0.7 to 2 eV. In contrast, the valence band is contributed mainly by Mo-$4d^4$ and Te-$5p^4$ orbitals with strong hybridization between Mo and Te in the valence band region from 0 to −0.5 eV. Similar calculations for the rhombohedral phase were performed and added in supplementary information as Fig. S5. Although there are some differences in the band structures, qualitative discussion remains unaffected. Furthermore, all structural parameters of r-GeTe and c-GeTe have been added to the supplementary information as Table S1.

2.4. TE transport properties

The temperature-dependent TE transport properties with varying Mo doping levels in the GeTe systems are presented in Fig. 6. The observed electrical conductivity (σ) decreases upon Mo doping and saturates when the doping level reaches 4% in the GeTe system (Fig. 6(a)). Mo atom substitution for Ge atoms would manifest a donor effect, driving a decrease in n from 8.28×10^{20} cm^{-3} for the pristine GeTe to 5.24×10^{20} cm^{-3} $Ge_{0.97}Mo_{0.03}Te$ (Table 1), may intimate the successful doping of Mo in the GeTe system. However, an increase in n for $Ge_{0.96}Mo_{0.04}Te$ may be due to the presence of the $MoTe_2$, intimating the beyond solubility limit of Mo in the GeTe system. The electrical conductivity and mobility for a semiconductor system is given by [10]:

$$\sigma = n\, e\, \mu, \quad \mu = e\tau/m^* \tag{1}$$

where n stands for charge carrier concentration, e for carrier charge, μ for carrier mobility, τ is the mean scattering time between the collisions, and m^* is the effective mass. The valence of $(Sb/Bi)^{3+}$ compared to Ge^{2+} ions plays an essential role in optimizing the n by contributing electrons to decrease the holes, which are the primary charge carriers in the GeTe system. As shown in Fig. 6(a), σ further reduces with the (Sb/Bi)-doping at 323 K, the σ of $Ge_{0.89}Mo_{0.01}Sb_{0.1}Te$ is only 9.3×10^4 S/m, and for $Ge_{0.89}Mo_{0.01}Bi_{0.1}Te$ is only 4.6×10^4 S/m, showing a striking decrease with that of pristine GeTe 7.84×10^5 S/m. Furthermore, an enhancement in σ with increasing temperature confers the degenerate semiconducting nature of all samples.

The Seebeck coefficient, S (Fig. 6(b)), shows a slight increase at RT, and the positive sign of S intimates the p-type character of semiconductors during the measured temperature range. Enhancement in S by adding Mo in the pristine GeTe at the room

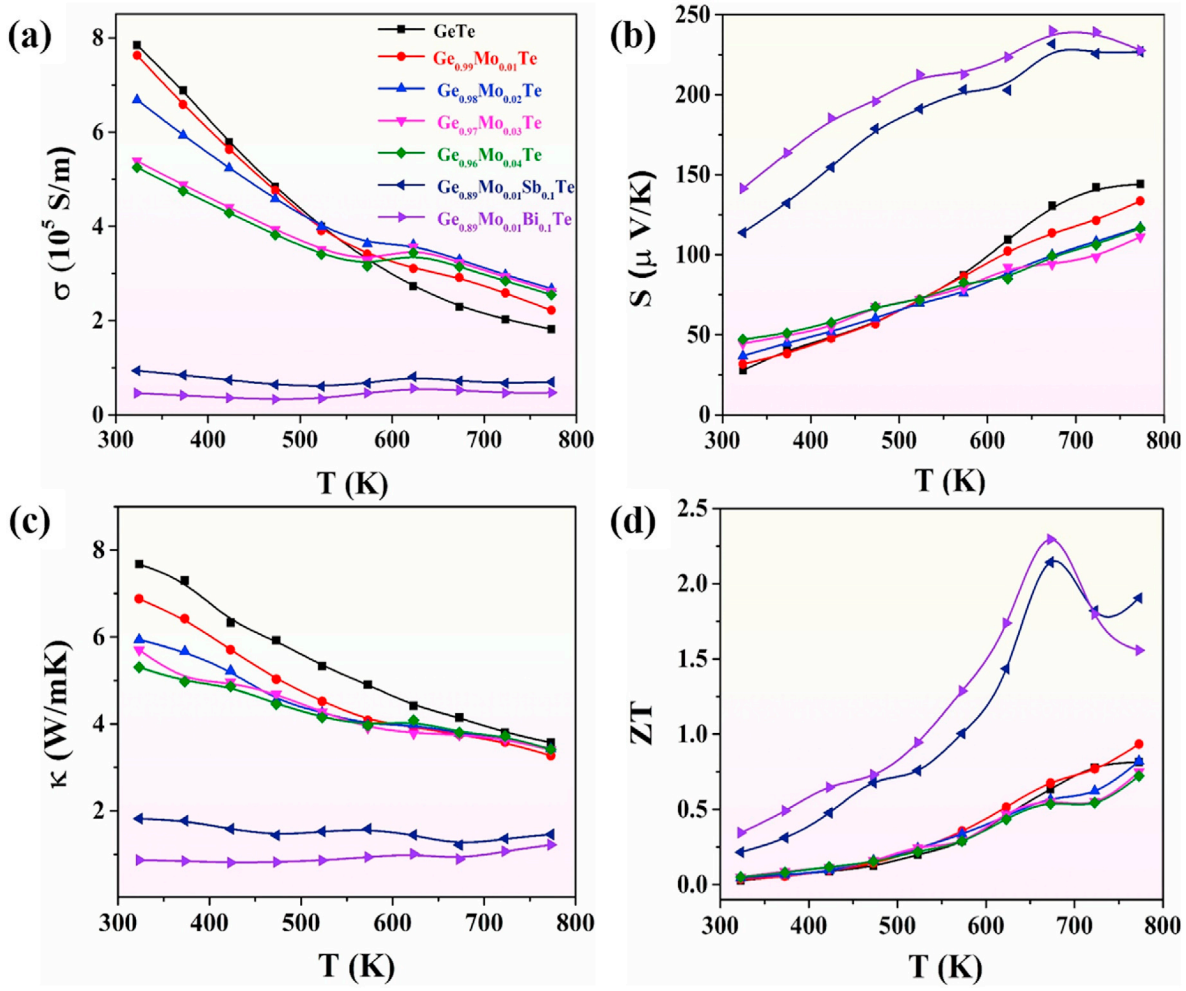

Fig. 6. Temperature-dependent TE transport properties of Mo doped GeTe systems; (a) electrical conductivity, (b) Seebeck coefficient, (c) total thermal conductivity, and (d) figure of merit, ZT.

Table 1
Thermoelectric transport properties of Mo doped GeTe systems at 323 K.

Sample	Carrier Concentration, n (x10 [20] cm^{-3})	Effective Mass (m*)	Mobility, μ ($cm^2 V^{-1}s^{-1}$)	σ (x10 [5] S/m)	S (μ V/K)	κ (W/mK)	Density (g/cm^3)
GeTe	8.28	1.13	58.83	7.84	27.82	7.68	6.04
$Ge_{0.99}Mo_{0.01}Te$	7.53	1.18	63.13	7.62	30.76	6.88	6.03
$Ge_{0.98}Mo_{0.02}Te$	6.07	1.22	68.65	6.68	36.79	5.94	6.07
$Ge_{0.97}Mo_{0.03}Te$	5.24	1.34	63.91	5.38	44.46	5.70	6.04
$Ge_{0.96}Mo_{0.04}Te$	5.75	1.50	56.89	5.24	47.02	5.30	6.05
$Ge_{0.89}Mo_{0.01}Sb_{0.1}Te$	0.94	1.09	62.21	0.93	113.75	1.82	6.13
$Ge_{0.89}Mo_{0.01}Bi_{0.1}Te$	0.86	1.27	33.36	0.46	141.38	0.87	6.38

temperature due to the enhancement of effective mass m^* and decreased n, agreeable with the equation (2). The reduction in the S at the high temperature may be attributed to the increased carrier concentration at elevated temperatures while transforming to cubic phase [62]. The Seebeck coefficient (S) is given by equation

$$S = \frac{8\pi^2 k_B^2}{3eh^2} m^* T \left(\frac{\pi}{3n}\right)^{2/3}, \quad S \propto \frac{m^*}{n^{2/3}} \tag{2}$$

where k_B is the Boltzmann's constant, h is the Planck's constant, with e, T, m^* and n are defined in equation (1). Furthermore, enhanced S in the entire temperature range upon Sb/Bi co-doping due to the primary reduction in n (Table 1) and a slight increase in effective mass. The maximum Seebeck coefficient of ~ 231 μV/K for the $Ge_{0.89}Mo_{0.01}Sb_{0.1}Te$ and ~ 240 μV/K for the $Ge_{0.89}Mo_{0.01}Bi_{0.1}Te$ is obtained at 673 K. A remarkable decrease in σ and a slight increase in S, the power factor (PF, σS^2), descends a little after Mo doping (Figure S6 a). In the case of Mo doped GeTe, there is no significant improvement in PF over pristine GeTe (high σ and low S). For the Bi/Sb co-doping cases, the PF maximum peak performance was around 673 K for $Ge_{0.89}Mo_{0.01}Bi_{0.1}Te$ and $Ge_{0.89}Mo_{0.01}Sb_{0.1}Te$ of ~3.03 × 10^{-3} W/m-K [2] and ~ 3.86 × 10^{-3} W/m-K [2], respectively. These peak performances in PF can be correlated with the phase transition temperatures.

The temperature-dependent thermal conductivity (κ) for the Mo doped GeTe is shown in Fig. 6(c). The overall thermal conductivity reduction is attributed to reduced electrical thermal conductivity (κ_{ele}) due to decreased n and lattice thermal conductivity (κ_{lat}) due to uniquely unveiled MCRs, high-density planar defects, grain boundaries, and point defects strengthening all-frequency phonon scattering. To further examine κ in the samples, we calculated the electronic thermal conductivity (κ_{ele}) and latticed thermal conductivity (κ_{lat}). The total thermal conductivity is denoted by:

$$\kappa = \kappa_{ele} + \kappa_{lat} \tag{3}$$

The electronic part of thermal conductivity is presented by equation [10]:

$$\kappa_{ele} = L_o \sigma T = n\, e\, \mu L_o T; \tag{4}$$

where $\boldsymbol{L_o}$ is Lorentz number. Fig. S6 (b) reveals both lattice as well as electronic thermal contributions calculated from Equations (3) and (4); the lattice contribution has systematically reduced due to more scattering of all-frequency phonons. However, a small electronic contribution has been attributed to its electron doping. Furthermore, Sb/Bi co-doping significantly decreases the lattice thermal conductivity due to the scattering effects and mass fluctuations of Ge/Mo/(Sb/Bi) and the scatterings unveiled by the microstructural analysis. Due to the significant variation in atomic size and mass among Bi and Ge compared to Sb and Ge, the Bi co-doped sample shows a relatively low value of κ. The lowest total thermal conductivity value, around 673 K for Sb/Bi substituted samples, is observed in the phase change transition range. All these phenomena lead to an ultra-low lattice thermal conductivity of κ_{lat} ~ 0.42 W $m^{-1}K^{-1}$ for $Ge_{0.89}Mo_{0.01}Sb_{0.1}Te$sample and ~ 0.32 W $m^{-1}K^{-1}$ for $Ge_{0.89}Mo_{0.01}Bi_{0.1}Te$ at 673 K, accelerating towards the theoretical minimum κ_{lat} of GeTe predicted by the diffusion model [70–72].

The temperature dependence of ZT values is illustrated in Fig. 6(d). Optimization of carrier concentration and decreased total thermal conductivity due to different scattering mechanisms mentioned above upon Mo doping in the GeTe System enhance the dimensionless figure of merit ZT. A maximum ZT of 0.93 is achieved at 773 K for $Ge_{0.99}Mo_{0.01}Te$, whereas co-doping of Sb/Bi leads to further enhanced thermoelectric ZT, as manifested in Fig. 6 (d). The maximum ZT ~ 2.14 is obtained for $Ge_{0.89}Mo_{0.01}Sb_{0.1}Te$, and ZT ~ 2.3 for $Ge_{0.89}Mo_{0.01}Bi_{0.1}Te$ at 673 K, an impressively high value than the pristine GeTe and Sb/Bi-doped GeTe system in this temperature range. The obtained ZT is one of the high values at 673 K compared to the previous work on transition elements doped systems [48,59–61]. Further optimized temperature-dependent TE properties of $Ge_{(0.9-x)}Mo_x(Sb/Bi)_{0.1}Te$ (x = 0.01, 0.02, 0.03) samples are discussed in Fig. S7. The optimized conditions were further reproduced and checked the electronic and thermal transport of the $Ge_{0.89}Mo_{0.01}Bi_{0.1}Te$ sample. Fig. S8 represents the reproduced properties within the error bar limit of each transport measurement. These results suggest that Mo acts as an extraordinary co-dopant along with Bi/Sb in the GeTe compound.

3. Conclusion

In summary, we extensively analyzed the unique role of Mo doping in the p-type GeTe system's thermoelectric properties with further co-doping of Sb/Bi. Mo decreases the p-type charge carriers as an electron donor, which is further optimized by Sb/Bi co-doping and increasing effective mass. Extensive investigations performed by advanced electron microscopy (FE-SEM and HR-TEM) have confirmed the presence of uniquely unveiled microcrystalline rods, dense grain boundaries, high-density planar defects, and point defects strengthening all-frequency phonon scattering to render an ultra-low κ. Finally, it leads to an ultrahigh peak ZT of ~2.3 at 673 K for the $Ge_{0.89}Mo_{0.01}Bi_{0.1}Te$ sample. Our present investigation could play an essential role in encouraging the intensive microstructure research of other similar materials, boosting TE performance in the mid-term temperature range. These outcomes present a unique path to search for new Pb-free and nature-friendly thermoelectric materials.

4. Experimental section

4.1. Sample preparation

We purchased the Germanium (Ge – 99.999%), Antimony (Sb –99.999%), Bismuth (Bi –99.999%), Molybdenum (Mo –99.95%), and Tellurium (Te – 99.999%) metals from the Sigma Aldrich. In highly evacuated (<4 × 10^{-4} Torr) quartz tubes, a series

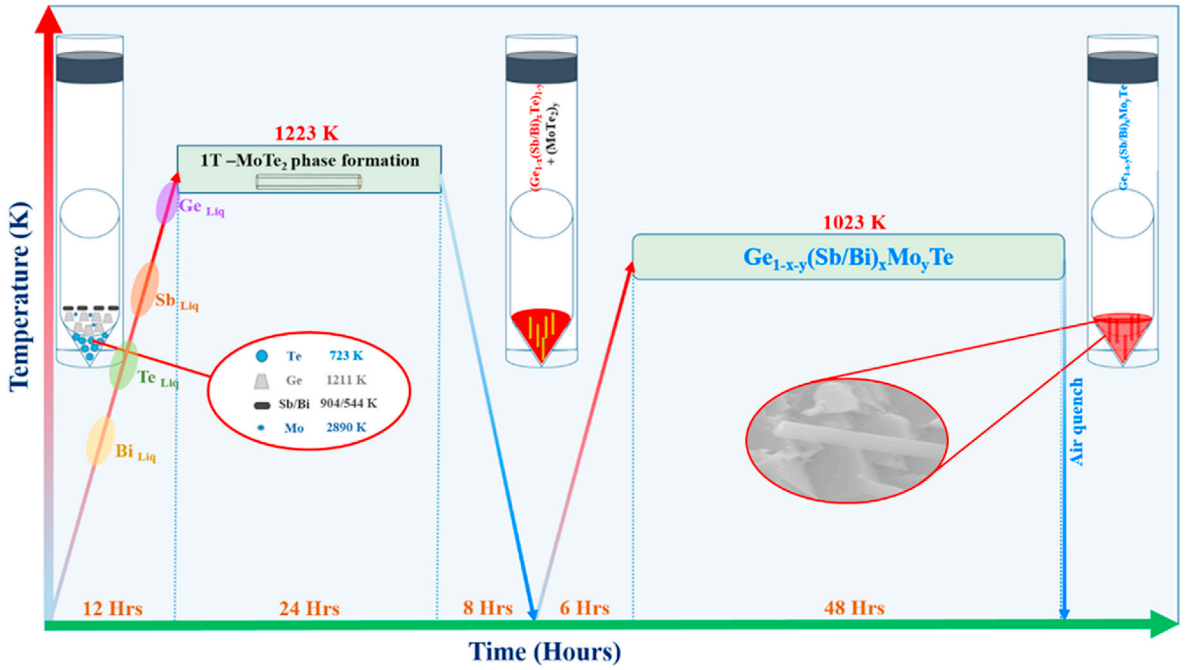

Fig. 7. Melt quench process of the $Ge_{1-x-y}(Sb/Bi)_xMo_yTe$ samples (detailed microcrystalline rod formation mechanism).

of samples in a precise stoichiometric ratio were sealed and kept at 1223 K for 24 h to form initial compositions. The cooled-down ingots were grounded in powder form and again sealed in a quartz tube to perform post-annealing at 1023 K for 48 h, further melting quenched in the air. The obtained ingots were grounded into fine powder for 1 h by hand milling. A graphite die of ~15 mm was used under a hot-press of 65 MP pressure at 800 K for 15 min in a high vacuum of $\sim 10^{-5}$ Torr to make the pellets. The conventional Archimedes method was used to measure the sintered pellets' densities and found them near >98% of the theoretical density, as mentioned in Table 1. The hot-pressed pellets were cut into rectangular pieces and square pieces for electrical transport and thermal diffusivity measurements.

4.2. Microcrystalline rods formation mechanism

The unique MCRs formation mechanism of the $Ge_{1-x-y}(Sb/Bi)_xMo_yTe$ samples during the two-step melt quenching process is shown in Fig. 7. All metal precursors of Ge, Sb, Bi, Te, and Mo were taken in a quartz tube with a precise stoichiometric ratio and sealed after purging in an Ar gas atmosphere 3 times to prevent the oxidation of the sample. After carefully examining all metal's binary phase diagrams (Ge—Te, Ge—Sb, Sb—Te, Ge—Bi, Bi—Te, Mo—Te, Mo—Ge, Mo—Sb, and Mo—Bi), we went through the synthesis process as follows. All metal precursors were initially melted at 1223 K with dwelling time for 24 h, driving all the materials to react and form their essential compounds during the first heating cycle. However, a high melting point of Mo led to its reaction with the Te compound initially, as observed in the phase diagram. Further MCRs formation will nucleate its growth as follows – (1) all the metal precursors were first dissolved at each melting point of individuals and start reacting to form its concerned compounds. (2) Mo reacts with the Te and forms its $MoTe_2$ phase at initials, and elevated temperature (1223 K) convert into its 1T′ phase (hexagonal rod). (3) During post sintering, which is above the melting point of GeTe will dissolve all the phases of Sb_2Te_3 and Bi_2Te_3. (4) Whereas $MoTe_2$ decomposed completely into the $Ge_{1-x}(Sb/Bi)_xTe$ liquid. (5) The sudden air quenching of the samples will lead to 1T′ nucleation-assisted MCRs formation with the elemental composition of the $Ge_{1-x-y}(Sb/Bi)_xMo_yTe$. (6) Further Mo solubility reached samples will start to form the secondary $MoTe_2$ phase formations as observed in $Ge_{0.97}Mo_{0.03}Te$ and $Ge_{0.96}Mo_{0.04}Te$ samples.

4.3. Structural and sample characterization

The synthesized powder sample's phase purity was identified utilizing Bruker D8 diffractometer, implemented with Cu K_α radiation ($\lambda = 1.5406$ Å). We investigated the temperature-dependent structural variations of the sample's synchrotron XRD in Taiwan Photon Source at the National Synchrotron Radiation Research Center (NSRRC) Taiwan. DSC profiles were collected using a METTLER TOLEDO, TGA/DSC 3+ (HT), keeping a 5 K min^{-1} heating rate under Ar atmosphere. We used FE-SEM equipped with EDS (JEOL JSM-6700F) to confirm the elemental compositions and distribution. High-Resolution Transmission Electron Microscope (HR-TEM) investigations utilizing the Tecnai G2 F30 STWIN TEM instrument with a field emission gun capacity of 200 kV were used to take the sample's microstructural pictures. All HR-TEM imaged on $Ge_{0.89}Mo_{0.01}Bi_{0.1}Te$ and $Ge_{0.89}Mo_{0.01}Sb_{0.1}Te$ samples with the TEM (JEM2100F, JEOL) with an acceleration voltage of 200 kV. The HR-TEM images and SAED patterns were analyzed by using the GATAN Digital Microscope software.

4.4. Computational data

To know the influence of Mo dopants on the TE properties of GeTe, ab-initio Density Functional Theory (DFT) calculations using the Quantum ESPRESSO package were implemented [73]. For the description of electron-ion interaction, we have used Ultra-soft pseudopotentials (USPP) with a kinetic energy and charge density cutoff of 680 eV and 6800 eV [74]. We have adopted generalized gradient approximation (GGA) with the Perdew-Burke-Ernzerhof (PBE) exchange-correlation functional [75]. The Brillouin zone was sampled using the Monkhorst—Pack scheme [76] of $4 \times 4 \times 4$

and 8 × 8 × 8 for relaxation and static calculations, respectively. Lattice vectors and atomic positions were fully relaxed to obtain the optimized configuration through the bfgs method. The DFT calculations were carried out on 5 × 5 × 4 supercells acquired from the c-GeTe (high-temperature phase).

4.5. Thermoelectric property measurements

The laser flash method (LFA 457, NETZSCH) regarding pyro Ceram standard calibration employing the Dulong–Petit law was used to measure the thermal diffusivity (D) and specific heat (C_p) of square pellets (thickness 2 mm and 6 mm diameter) with ~ 7% uncertainty. $\kappa = D\, C_p\, \rho$ and $\kappa_{lat} = \kappa - \kappa_{ele}$ was used to calculate the κ, and κ_{lat}, respectively. The Wiedemann–Franz law, $\kappa_{ele} = L_o\, \sigma\, T$, was used to calculate the κ_{ele}, where L_o is the Lorenz number calculated by an empirical equation of 1.5 + exp (-|S|/116). For the carrier transport properties, σ and S were measured concurrently on ZEM-3, ULVAC under He gas environment using polished pellet ~ ($2 \times 2 \times 14\ mm^3$) with ~ 5% uncertainty. PPMS AC transport 5-point probe measurement in a magnetic field of up to 5 T used to determine the Hall coefficient (R_h). Equations, $n = 1/(eR_h)$ and $\mu = \sigma R_h$, were used to determine the carrier concentration (n) and mobility (μ) with ~ 3% uncertainty, respectively, whereas e denotes the electron charge. To enhance the figures' clarity, error bars have not been displayed.

Authors contributions

R.S. and F-L L. supervised the project. S.I. conceived the idea, designed the experiments, and analyzed the data. M.U. and B·S.P. performed DFT calculations and interpreted the data. K.S. HR-TEM and PPMS measurements. S.I., K·S., F-L. L. and R.S. reviewed and edited the manuscript before submission. RS, FL, YY, LC, & KH scientific discussion. All the authors made substantial contributions to the discussion of the content.

Declaration of competing interest

The authors declare that they have no known competing financial interests or personal relationships that could have appeared to influence the work reported in this paper.

Acknowledgments

Safdar Imam acknowledges the MOE Taiwan scholarship for financial support. The authors acknowledge the project grant of thermoelectric material for sustainable energy project: AS-SS-109-01. RS acknowledges the financial support provided by the Ministry of Science and Technology in Taiwan under project number MOST-110-2112-M-001-065-MY3 and Academia Sinica for the budget of AS-iMATE-109-13. The authors are thankful to Taiwan Photon Source (TPS), situated at the National Synchrotron Radiation Research Center (NSRRC), for studying temperature-dependent synchrotron X-ray diffraction (XRD) data. M Ubaid and BS Pujari thank National PARAM Supercomputing Facility at the Centre for Development of Advanced Computing, Pune, for computing support.

Appendix A. Supplementary data

Supplementary data to this article can be found online at https://doi.org/10.1016/j.mtphys.2021.100571.

References

[1] N. Nandihalli, et al., Nanomater. Energy (2020) 105186.
[2] T. Mori, S. Priya, MRS Bull. 43 (3) (2018) 176.
[3] F.J. DiSalvo, Science 285 (5428) (1999) 703.
[4] Y.-J. Lin, et al., Nat. Commun. 12 (1) (2021) 1.
[5] K. Biswas, et al., Nature 489 (7416) (2012) 414.
[6] I. Petsagkourakis, et al., Sci. Technol. Adv. Mater. 19 (1) (2018) 836.
[7] M. Zebarjadi, et al., Energy Environ. Sci. 5 (1) (2012) 5147.
[8] L.-D. Zhao, et al., Science 351 (6269) (2016) 141.
[9] W. Liu, et al., Nanomater. Energy 1 (1) (2012) 42.
[10] G.J. Snyder, E.S. Toberer, Nat. Mater. 7 (2) (2008).
[11] T. Zhu, et al., Adv. Mater. 29 (14) (2017) 1605884.
[12] B. Yu, et al., Nano Lett. 12 (4) (2012) 2077.
[13] M. Zebarjadi, et al., Nano Lett. 11 (6) (2011) 2225.
[14] A. Banik, K. Biswas, J. Mater. Chem. 2 (25) (2014) 9620.
[15] Y. Pei, et al., Nature 473 (7345) (2011) 66.
[16] W. Liu, et al., Phys. Rev. Lett. 108 (16) (2012) 166601.
[17] L.-D. Zhao, et al., Energy Environ. Sci. 6 (11) (2013) 3346.
[18] C. Fu, et al., Energy Environ. Sci. 8 (1) (2015) 216.
[19] F. Ahmed, et al., J. Mater. Chem. 5 (16) (2017) 7545.
[20] R. Ang, et al., Angew. Chem. 127 (44) (2015) 13101.
[21] L.D. Hicks, M.S. Dresselhaus, Phys. Rev. B 47 (19) (1993) 12727.
[22] Z. Liu, et al., Proc. Natl. Acad. Sci. Unit. States Am. 115 (21) (2018) 5332.
[23] Y. Qiu, et al., J. Mater. Chem. 7 (46) (2019) 26393.
[24] R. Nunna, et al., Energy Environ. Sci. 10 (9) (2017) 1928.
[25] Y. Liu, et al., Advanced Energy Materials 6 (9) (2016) 1502423.
[26] X. Meng, et al., Advanced Energy Materials 7 (13) (2017) 1602582.
[27] S.H. Lo, et al., Adv. Funct. Mater. 22 (24) (2012) 5175.
[28] J. Yang, et al., Appl. Phys. Lett. 85 (7) (2004) 1140.
[29] L.-D. Zhao, et al., Nature 508 (7496) (2014) 373.
[30] M.K. Jana, et al., Angew. Chem. 128 (27) (2016) 7923.
[31] D. Morelli, et al., Phys. Rev. Lett. 101 (3) (2008): 035901.
[32] C.W. Li, et al., Nat. Phys. 11 (12) (2015) 1063.
[33] P. Qin, et al., J. Mater. Res. 32 (16) (2017) 3029.
[34] G. Zhu, et al., Nanomater. Energy 2 (6) (2013) 1172.
[35] J.R. Gandhi, et al., CrystEngComm 20 (41) (2018) 6449.
[36] X. Zhang, et al., Joule 4 (5) (2020) 986.
[37] S. Perumal, et al., J. Mater. Chem. C 4 (32) (2016) 7520.
[38] J. Li, et al., Joule 2 (5) (2018) 976.
[39] J. Li, et al., NPG Asia Mater. 9 (3) (2017) e353.
[40] K.S. Bayikadi, et al., J. Mater. Chem. 7 (25) (2019) 15181.
[41] M. Hong, et al., Adv. Mater. 30 (11) (2018) 1705942.
[42] S. Perumal, et al., Inorganic Chemistry Frontiers 3 (1) (2016) 125.
[43] S. Perumal, et al., Chem. Mater. 27 (20) (2015) 7171.
[44] K.S. Bayikadi, et al., J. Mater. Chem. 8 (10) (2020) 5332.
[45] Y. Gelbstein, J. Davidow, Phys. Chem. Chem. Phys. 16 (37) (2014) 20120.
[46] L. Wu, et al., NPG Asia Mater. 9 (1) (2017) e343.
[47] B. Srinivasan, et al., Materials 11 (11) (2018) 2237.
[48] J. Shuai, et al., Small 16 (13) (2020) 1906921.
[49] B. Srinivasan, et al., J. Phys. Chem. C 122 (1) (2018) 227.
[50] Z. Zheng, et al., J. Am. Chem. Soc. 140 (7) (2018) 2673.
[51] J. Li, et al., Chem. Mater. 29 (2) (2017) 605.
[52] J. Shuai, et al., Materials Today Physics 9 (2019) 100094.
[53] S. Perumal, et al., Joule 3 (10) (2019) 2565.
[54] S. Perumal, et al., Chem. Mater. 29 (24) (2017) 10426.
[55] M. Hong, et al., Advanced Energy Materials 8 (30) (2018) 1801837.
[56] B. Srinivasan, et al., Inorganic Chemistry Frontiers 6 (1) (2019) 63.
[57] J. Li, et al., J. Am. Chem. Soc. 140 (47) (2018) 16190.
[58] M. Hong, et al., J. Am. Chem. Soc. 141 (4) (2018) 1742.
[59] B. Srinivasan, et al., J. Mater. Chem. 8 (38) (2020) 19805.
[60] W. Gao, et al., Appl. Phys. Lett. 118 (3) (2021): 033901.
[61] Q. Sun, et al., Advanced Energy Materials 11 (20) (2021) 2100544.
[62] M. Sist, et al., Phys. Rev. B 97 (9) (2018): 094116.
[63] W.D. Liu, et al., Advanced Energy Materials 10 (19) (2020) 2000367.
[64] T. Zhu, et al., ACS Appl. Mater. Interfaces 11 (44) (2019) 41472.
[65] B. Khasimsaheb, et al., Curr. Appl. Phys. 17 (2) (2017) 306.
[66] D. Guo, et al., J. Phys. Chem. C 117 (41) (2013) 21597.
[67] R. Al Rahal Al Orabi, et al., Chem. Mater. 28 (1) (2016) 376.
[68] H. Ming, et al., ACS Appl. Mater. Interfaces 12 (17) (2020) 19693.
[69] G. Xing, et al., J. Appl. Phys. 123 (19) (2018) 195105.
[70] M.T. Agne, et al., Energy Environ. Sci. 11 (3) (2018) 609.
[71] T. Xing, et al., Adv. Mater. 33 (17) (2021) 2008773.
[72] L. Yue, et al., ACS Appl. Energy Mater. 2 (4) (2019) 2596.
[73] P. Giannozzi, et al., J. Phys. Condens. Matter 21 (39) (2009) 395502.
[74] D. Vanderbilt, Phys. Rev. B 41 (11) (1990) 7892.
[75] J.P. Perdew, et al., Phys. Rev. Lett. 77 (18) (1996) 3865.
[76] H.J. Monkhorst, J.D. Pack, Phys. Rev. B 13 (12) (1976) 5188.